IEEE Robotics and Automation Letters (RA-L) paper, presented at ICRA 2026, Vienna, Austria. Cite as RA-L paper.

Safety-Aware UAV Formation Scheme for Guiding UGVs Through Obstacle-Laden Environments

Ruikang Xiao, Shuting Wang, Yuanlong Xie, *Senior Member, IEEE*, Youmin Zhang, *Fellow, IEEE*, and Sheng Quan Xie, *Fellow, IEEE*

***Abstract*—Using uncrewed aerial vehicle (UAV) formations to guide uncrewed ground vehicles (UGVs) through unstructured obstacle-laden areas leads to highly efficient execution of tasks such as the transportation of supplies. However, existing methods fail to efficiently plan obstacle-avoidance strategies for the entire UAV-UGV swarm. Additionally, the formation controller and planner are isolated, resulting in the degradation of formation tracking accuracy, which presents potential security risks. This paper proposes a novel UAV formation scheme that integrates safe corridor (SC) generation, trajectory fitting, and formation tracking to ensure operational safety. The scheme employs a novel line-of-sight (LOS) mechanism to optimize A*-planned waypoints, generating the SC as an obstacle-avoidance strategy. A minimum snap trajectory is fitted to the optimized waypoints with SC constraints. Bridged by the trajectory, the scheme develops a rigid-graph-based controller (RGC) to track the planning result, enabling dynamic formation maneuvering within the SC. Consequently, the proposed UAV formation scheme achieves obstacle-avoidance guidance by restricting the UGVs to the formation projection. The validation results demonstrate that the proposed scheme exhibits enhanced robustness and superior planning capabilities compared to traditional methods.**

***Index Terms*—Formation tracking, obstacle avoidance, safe corridor (SC), uncrewed aerial vehicle (UAV).**

I. Introduction

IN INDUSTRIAL and military applications, heterogeneous uncrewed swarm systems demonstrate enhanced flexibility and efficiency through their collaborative capabilities [1]. Within these systems, the collaboration between uncrewed aerial vehicles (UAVs) and uncrewed ground vehicles (UGVs) plays a crucial role [2]. For a UAV-UGV swarm shown in Fig. 1, the UAV formation can guide UGVs to avoid obstacles by constraining UGVs to the projection of the formation [3]. As exemplified by the supply transportation task in obstacle-laden areas, onboard sensors of UGVs are prone to environmental misjudgment in these complex terrains, which may lead to the entrapment of the UGVs. In contrast, UAV formations perform rapid environmental reconnaissance and collaboratively guide UGVs through obstacle-laden areas, significantly improving both operational efficiency and transportation safety. Therefore, a UAV-guided formation scheme that emphasizes safety is urgently needed, including an efficient obstacle-avoidance strategy and a robust formation control mechanism.

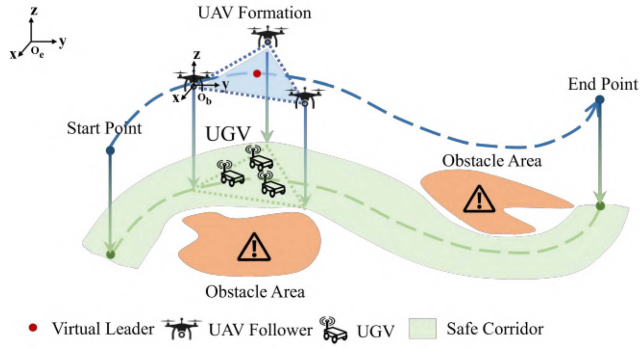

Fig. 1. Schematic of a UAV formation guiding UGVs.

Regarding UAV formation control, researchers have developed various strategies such as the virtual structure approach [4], the leader-follower approach [5], the behavior-based approach [6], the consensus-based approach [7], and the artificial potential field (APF) approach [8]. As demonstrated in [5], the leader-follower approach effectively maintains formation by assigning hierarchical roles to visibility-constrained mobile robots. The virtual structure approach allows UAVs to maintain rigid formation geometry, enabling agile and precise maneuvers such as interleaved swarm operations [4]. The behavior-based approach offers decentralized control as in [6], [9]. However, these approaches are predominantly designed for obstacle-free environments [10], limiting their applicability in the real world, where UAVs need to guide UGVs in unstructured obstacle-laden environments. Therefore, a path-planning algorithm is needed to provide obstacle-avoidance strategies for UAV formations.

Research on path planning for UAV formations has advanced significantly, including global and local planning strategies. Global path planning generates optimal paths from an initial point to a destination in static or well-mapped environments [11], [12], [13]. Conversely, by focusing on the immediate surroundings, local strategies enable UAV formations to react to unforeseen obstacles or changes in the operational area [14], [15],

Received 11 January 2025; accepted 8 May 2025. Date of publication 23 May 2025; date of current version 2 June 2025. This article was recommended for publication by Associate Editor Z. Kingston and Editor A. Bera upon evaluation of the reviewers' comments. This work was supported in part by the National Natural Science Foundation of China under Grant U21A20151 and Grant 52275488, and in part by the Key Research and Development Program of Hubei Province, China under Grant 2022BAA064. *(Corresponding author: Yuanlong Xie.)*

Ruikang Xiao, Shuting Wang, and Yuanlong Xie are with the School of Mechanical Science and Engineering, Huazhong University of Science and Technology, Wuhan 430074, China (e-mail: ruikangxiao@hust.edu.cn; wangst@hust.edu.cn; yuanlongxie@hust.edu.cn).

Youmin Zhang is with the Department of Mechanical, Industrial and Aerospace Engineering, Concordia University, Montréal, QC H3G 1M8, Canada (e-mail: youmin.zhang@concordia.ca).

Sheng Quan Xie is with the School of Electrical and Electronic Engineering, University of Leeds, LS1 3EY Leeds, U.K. (e-mail: S.Q.Xie@leeds.ac.uk).

Digital Object Identifier 10.1109/LRA.2025.3572826

IEEE Robotics and Automation Letters (RA-L) paper, presented at ICRA 2026, Vienna, Austria. Cite as RA-L paper.

[16]. For example, Liu et al. proposed a trajectory generation algorithm based on the concept of the safe flight corridor (SFC) [17]. In [18], the method to generate the minimum snap trajectories for a single UAV was proposed. However, existing studies often concentrate on developing independent paths for each UAV within the formation, thus ignoring the general stability of the formation [19], [20]. This oversight leads to challenges in the generation of obstacle-avoidance strategies. Furthermore, conventional formation control methods struggle to seamlessly integrate obstacle-avoidance strategies for the formation [21].

All these issues result in safety risks of UAV formations. Therefore, an integrated UAV formation scheme is required to effectively bridge the gap between obstacle avoidance and formation control. This can be accomplished by leveraging a fitted trajectory as a shared reference.

Given the limitations mentioned above, this paper proposes a novel safety-aware UAV formation scheme. The main contributions are as follows:

1) A trajectory-bridged UAV formation scheme is proposed that includes a safe corridor (SC) planner and a formation controller to address the challenge for UAV formation to safely guide UGVs through obstacle-laden environments. In contrast to the previous method [22], [23], the proposed method is based on a rigid graph structure, thus requiring less computational resources and enhancing real-time responsiveness.
2) An SC planning method for UAV formation based on an improved A* algorithm is proposed, incorporating a novel line-of-sight (LOS) mechanism to generate the optimal waypoints. Unlike previous obstacle-avoidance strategies for each UAV in the formation [11], [14], this method considers the obstacle avoidance for the whole formation, ensuring a stable formation configuration.
3) A rigid-graph-based controller (RGC) is proposed for UAV formation to track the trajectory while incorporating SC information. Unlike current methods that directly control the formation size [24], this controller dynamically adjusts the formation using the planned SC, improving the tracking stability and smoothness of obstacle avoidance of the formation.

The remainder of this paper is as follows: Section II establishes the UAV dynamic model and clarifies the formation control objective. Section III details the implementation of the proposed formation scheme. Section IV validates the effectiveness of the proposed scheme. Section V concludes the paper and outlines future research directions.

II. Problem Formulation

A. UAV Model

The UAV discussed in this paper is a quadrotor, and the positional dynamics of the UAV in the earth coordinate system O_e is considered as

$$\begin{bmatrix} \ddot{x} \\ \ddot{y} \\ \ddot{z} \end{bmatrix} = \begin{bmatrix} 0 \\ 0 \\ g \end{bmatrix} + \frac{1}{M}(\boldsymbol{R}_e^b)^{-1} \begin{bmatrix} 0 \\ 0 \\ -U \end{bmatrix}, \tag{1}$$

where U represents the total external force acting on the UAV, M is the UAV's take-off mass, $\boldsymbol{R}_e^b$ is the rotation matrix between O_e and the body coordinate system O_b.

Similarly, by defining the pitch angle as ϕ, the roll angle as θ, and the yaw angle as ψ, the UAV attitude dynamics model is denoted as

$$\begin{bmatrix} \ddot{\phi} \\ \ddot{\theta} \\ \ddot{\psi} \end{bmatrix} = \boldsymbol{I}^T \begin{bmatrix} \tau_x + w_\theta w_\psi (I_y - I_z) - J_0 w_\theta N \\ \tau_y + w_\theta w_\psi (I_z - I_x) - J_0 w_\phi N \\ \tau_z + w_\phi w_\theta (I_x - I_y) \end{bmatrix}, \tag{2}$$

where $\boldsymbol{I}$ represents the rotational inertia along each axis of the UAV, and τ denotes the torque generated by the propeller thrust on the body axis. J_0 denotes the total rotational inertia of the motor rotor and propeller. Furthermore, $\boldsymbol{w}$ refers to the angular velocity of the UAVs along each axis, and N is the sum of the rotational speeds of the propellers.

B. Formation Model

Consider a formation with n UAVs in a space of m dimensions, and let $\boldsymbol{p}_i \in \mathbb{R}^m$ represent the position of the i-th UAV in O_e. The UAV formation is defined by a frame $F = (G, \boldsymbol{p})$, where $\boldsymbol{p} = [\boldsymbol{p}_1, \ldots, \boldsymbol{p}_n] \in \mathbb{R}^{nm}$ denotes the positions of all UAVs. Here, $G = (V, E)$ is an undirected graph, where V is the vertex set with each vertex corresponding to a UAV and the edge set E represents the distance constraints between UAVs.

With this framework, the formation is mathematically characterized by the edge function $\phi : \mathbb{R}^{nm} \to \mathbb{R}^l$, where $l = \frac{n(n-1)}{2}$. This function computes the squared distances between UAV pairs as $\phi(\boldsymbol{p}) = [\ldots, \|\boldsymbol{p}_a - \boldsymbol{p}_b\|^2, \ldots]$, for $(a, b) \in E$, where $\boldsymbol{p}_a$ and $\boldsymbol{p}_b$ denote the current global coordinates of the UAVs in the formation.

This setup implies that knowledge of all pairwise distances within the formation F determines the graph G to be a rigid graph. A rigid graph G ensures that the relative positions of its vertices remain fixed under certain conditions, resulting in a stable formation.

The rigidity matrix $\boldsymbol{R} : \mathbb{R}^{nm} \to \mathbb{R}^{l \times nm}$ is defined as

$$\boldsymbol{R}(\boldsymbol{p}) = \frac{1}{2} \frac{\partial \phi(\boldsymbol{p})}{\partial \boldsymbol{p}}. \tag{3}$$

For the edges between vertices a and b, the corresponding row of the rigidity matrix is given by

$$\left[0, \ldots, 0, (\boldsymbol{p}_a - \boldsymbol{p}_b)^T, 0, \ldots, 0, (\boldsymbol{p}_b - \boldsymbol{p}_a)^T, 0, \ldots, 0\right] \tag{4}$$

For a formation $F \subseteq \mathbb{R}^m$, the graph G is rigid if and only if [25]: $rank(\boldsymbol{R}(\boldsymbol{p})) = mn - \frac{m(m+1)}{2}$. This condition implies that a 2D formation with n UAVs achieves minimal rigidity when exactly $2n - 3$ distance constraints are enforced.

C. Control Objective

Before delving into further detail of the formation scheme, it is necessary to introduce the fundamental assumptions underlying this problem. In this paper, the asterisk $(*)$ is used as a superscript to denote the ideal situation of formation. For example, the ideal formation framework is defined as F^*.

Assumption 1: The formation and sensor graph are identical, denoted as $G_s = G^*$.

Assumption 2 ([26]): Inter-agent connectivity within the formation is consistently maintained, ensuring that each UAV remains in the communication range of any UAVs in its neighbor set E^*.

Assumption 3 ([27]): Initially, the UAVs fail to meet the required inter-agent distance constraints. such that $\|\boldsymbol{p}_a(0) -$

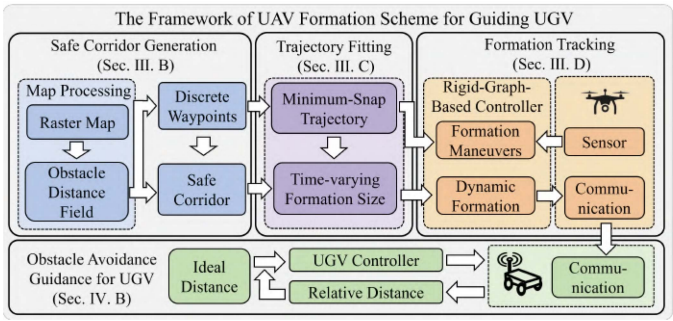

Fig. 2. The framework of the proposed scheme.

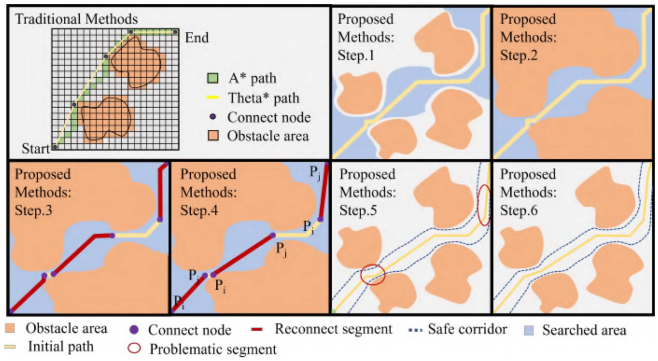

Fig. 3. Comparison of traditional path planning algorithms and generation process of the SC.

Algorithm 1: SC Generating and Trajectory Fitting.

Input: Rasterized map $\mathbf{M_0}$, Obstacle distance field $\mathbf{F_o}$, Formation center $\boldsymbol{p_g}(\mathbf{t})$, goal point $\boldsymbol{P_e}$
Output: Formation trajectory $\mathbf{T_r}(\mathbf{t})$, Safe corridor $\mathbf{F_r}(\mathbf{t})$
while $\boldsymbol{p}_g(t) \neq \boldsymbol{P}_e$ **do**
$(M_k, W_{ini}) = \mathbf{genAstar}(M_0, F_o, \boldsymbol{p}_g(t), \boldsymbol{P}_e)$;
$W_{opt} = \mathbf{optRecon}(M_k, W_{ini}, F_o, \boldsymbol{p}_g(t), \boldsymbol{P}_e)$;
$(C_{wp}, W_{fin}) = \mathbf{genCorridor}(W_{opt}, M_0, F_o)$;
$T_r(t) = \mathbf{optWP}((W_{fin}, \boldsymbol{p}_g(t), \boldsymbol{P}_e))$;
$F_r(t) = \mathbf{genFormation}(T_r(t), C_{wp})$;
end while
return $(F_r(t), T_r(t))$;

$\boldsymbol{p}_b(0)\| \neq d_{ab}$, for all $a, b \in V^*$, where d_{ab} represents the desired distance between UAVs a and b.

The formation control is based on the relative positioning of the UAVs. Specifically, the desired distance between the UAVs a and b in the ideal formation is defined as $d_{ab} = \|\boldsymbol{p}_a^* - \boldsymbol{p}_b^*\| > 0$, for $a, b \in V$.

Initially, the UAVs start from chaotic initial positions and move to form a predefined formation, known as formation acquisition. During this phase, the distances between any two UAVs, a and b, are expected to converge to d_{ab}, i.e., $\|\boldsymbol{p}_a(t) - \boldsymbol{p}_b(t)\| \to d_{ab} as\ t \to \infty$. Since the formation is required to guide the UGVs through obstacle-laden areas by dynamically adjusting its size, d_{ab} becomes time-varying during operation and is expressed as $d_{ab}(t)$. Consequently, the dynamic formation process is described as $\|\boldsymbol{p}_a(t) - \boldsymbol{p}_b(t)\| \to d_{ab}(t)$ as $t \to \infty$. While achieving dynamic formation, the UAV formation must simultaneously follow a planned trajectory to navigate from the beginning to the end. This behavior is quantified as $\|\dot{\boldsymbol{p}}_a(t) - \boldsymbol{v}_{da}(t)\| \to 0 as t \to \infty$, where $a = 1, \ldots, n$, and $\boldsymbol{v}_{da}(t)$ indicates the desired maneuvering speed of the UAV a.

In summary, the objectives of the controller are defined as

$$\begin{cases} \|\boldsymbol{p}_a(t) - \boldsymbol{p}_b(t)\| \to d_{ab}(t) \quad as \quad t \to \infty \\ \|\dot{\boldsymbol{p}}_a(t) - \boldsymbol{v}_{da}(t)\| \to 0 \quad as \quad t \to \infty. \end{cases} \tag{5}$$

III. Methodology

A. Overview

The framework of the proposed scheme is depicted in Fig. 2 and its execution process is outlined in Algorithm 1. First, within the global map M_0, the function **genAstar** generates an initial set of sparse waypoints W_{ini}, spanning from the formation center $\boldsymbol{p}_g(t)$ to the goal point $\boldsymbol{P}_e$, based on the obstacle distance field F_o. Then, during this process, the explored region M_k is recorded within M_0. Next, the function **optRecon** performs waypoints reconnection based on M_k and W_{ini}, resulting in an optimized path W_{opt}. To ensure a safe distance from the obstacles, the function **genCorridor** considers F_o and laterally extends W_{opt} within M_0, forming the SC, and C_{wp}. Then, this safe corridor is used to guide UAV-UGV formations to avoid obstacles. The function **optWP** applies polynomial fitting to W_{opt}, producing the formation tracking trajectory $T_r(t)$. Finally, the function **genFormation** calculates the UAV dynamic formation plan $F_r(t)$, which is derived using $T_r(t)$ and C_{wp}. This formation plan represents the proportional size of the UAV formation relative to its original size at any given moment.

B. SC Generation

In SC generation, the map is first rasterized to produce an obstacle distance field. Then, the A* algorithm is used, generating the initial waypoints. The heuristic function h incorporates the obstacle distance field F_o and is expressed as $h = \sqrt{\|\boldsymbol{P} - \boldsymbol{P}_e\|^2} + k(r_F - F_o(\boldsymbol{P}))^q$, where k and q are the weight coefficients that control the influence of F_o within the heuristic function, and r_F is a user-defined distance threshold in the obstacle distance field F_o. In the rasterized map, for any grid point $\boldsymbol{P}$ with a distance to the nearest obstacle greater than or equal to r_F, $F_o(\boldsymbol{P})$ is set to r_F.

As illustrated in Fig. 3, the A* algorithm generates suboptimal waypoints due to constraints of the grid structure. In contrast, the waypoints produced by the Theta* algorithm, which utilizes LOS detection, are significantly shorter. However, the Theta* algorithm does not account for obstacle proximity, which can lead to waypoints that are too close to obstacles. Expanding the obstacles can reduce this risk, but it may render the Theta* algorithm ineffective in obstacle-laden areas. To overcome the limitations of the A* algorithm and Theta*, a novel LOS detection method is introduced that integrates the obstacle distance field in the SC generation process.

The proposed SC generation method involves six steps, as highlighted in Fig. 3. First, the A* algorithm performs an initial waypoint planning, recording the searched area F_s, as shown in blue. Next, the remaining map area is designated as the obstacle area F_b to generate the map M_k for LOS detection. In the third step, the waypoint segments that require reconnection are identified, which is based on the ratio of F_s to F_b within a certain distance around the waypoints. Once the ratio surpasses the predetermined threshold, it implies that a sufficient area has

been explored. At this stage, for the red segments in Fig. 3, reconnection is necessary.

In the fourth step, LOS detection is initiated. Each waypoint segment that requires reconnection consists of two connected nodes: $\boldsymbol{P}_i$ as the start and $\boldsymbol{P}_j$ as the end. Using the Bresenham algorithm, an approximate straight line is drawn between $\boldsymbol{P}_i$ and $\boldsymbol{P}_j$. If the line intersects an obstacle, the next point in the waypoint segment becomes the new starting point, and the process is repeated. Once LOS detection succeeds, the current starting point becomes the new end, and $\boldsymbol{P}_i$ resumes as the starting point, continuing the process until $\boldsymbol{P}_i$ becomes the end of the next LOS detection. Additionally, the LOS detection is restricted to the area explored previously, further ensuring safety. In the fifth step, the waypoints are extended to form the SC for formation. The updated boundary B_k in the k-th iteration is computed as

$$B_k = \left(\bigcup_{\boldsymbol{P} \in B_{k-1}} D\left(\boldsymbol{P}\right) \right) \setminus \left(\bigcup_{i=0}^{k-1} B_i \cup \{\boldsymbol{P} | F_o\left(\boldsymbol{P}\right) < d_{\min}\} \right), \tag{6}$$

where $d_{\min}$ denotes the minimum safe distance threshold for the formation system, and $D(\boldsymbol{P})$ represents the neighborhood generation operator. Upon reaching the predefined number of iterations n, the final safe corridor boundary is defined as $C_{wp} = B_n$, and the safe region is formulated as $R_s = \bigcup_{i=0}^{n} B_i$. In the sixth step, the proposed scheme adjusts the waypoints within the SC to ensure they strictly adhere to the central axis of the corridor. In this process, R_s serves as the rasterized map, and a boundary-aware distance field F_u is constructed along C_{wp}. F_u is integrated into the heuristic function of the A* algorithm for path re-planning, thereby yielding the adjusted waypoint set W_{fin}.

Remark 1: The proposed novel LOS detection method generates shorter waypoints compared to the A* algorithm and ensures that the waypoints maintain a safe distance from obstacles, ultimately enabling the generation of high-quality SC. Different from the method proposed in [28], the proposed novel LOS mechanism significantly shortens the waypoints. In contrast to the traditional LOS mechanism mentioned in [29], the novel LOS mechanism optimizes the reconnected waypoints by incorporating obstacle distance field information.

C. Trajectory Fitting

To establish a smooth connection between SC information and the controller, a trajectory is fitted to the waypoints derived from the SC generation process. The trajectory provides time-varying formation size information and the motion data for the formation to track. The initial phase involves waypoint sampling to obtain trajectory-fitting nodes. A gradient sampling strategy is proposed to integrate obstacle distance field information to minimize information loss during sampling, applying higher density to nearby obstacles and lower density to obstacles-free regions. The sampling density indicator formula is given by $\lambda_i = \min(\frac{s\omega}{F_o(W_{opt}(i))}, 1)$, where s is a positive constant that globally regulates the magnitude of λ_i, and ω denotes a dynamic scaling factor that normalizes $\frac{1}{F_o(W_{opt}(i))}$ to the range [0,1].

Polynomial trajectories are represented as: $T_r(t) = \sum_{i=0}^{n} T_i t^i$, where $T_r(t)$ represents the formation center's trajectory, and T_i denotes the polynomial coefficients.

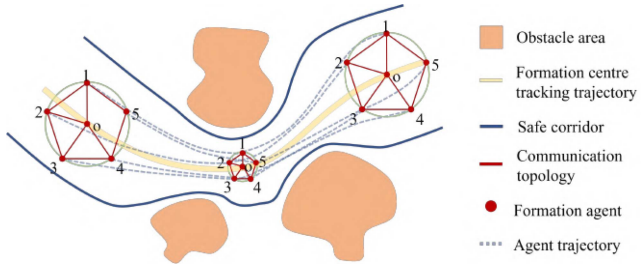

Fig. 4. Dynamic formation processes of UAV formation that guide UGVs.

To ensure the trajectory's trackability, smooth transitions must be maintained between consecutive segments and the trajectory must strictly pass through all designated nodes. For a trajectory parameterized by n-segment polynomials, how to determine its coefficient set $T = \{T_i\}_{i=1}^{n}$ becomes a constrained optimization problem and is formulated as

$$\min_{T} \sum_{i=1}^{k} \int_{i-1}^{i} \left(T_r^{(4)}(t) \right)^2 dt. \tag{7}$$

After obtaining $T_r(t)$, a dynamic formation plan, denoted as $F_r(t)$, is provided for the formation controller based on $T_r(t)$ and C_{wp}. As shown in Fig. 4, the UAV formation with a virtual leader o adopts a regular pentagon. The formation's minimal enclosing circle is constructed, taking o as the center and r as the radius. Initially, when the formation is far from obstacles, the circle's radius is maximized, denoted as $r_{\max}$. During the operation, the minimum distance between o and the edge of the SC is calculated, represented as $d_{\min}(T_r(t_i))$. When $d_{\min}(T_r(t_i)) < r_{\max}$, the formation is too close to the edges of the SC; thus, adjust the radius to $r = cd_{\min}$, where c is a positive constant less than 1. Consequently, the dynamic formation plan is given by $F_r(t) = \frac{cd_{\min}(T_r(t))}{r_{\max}}$.

Remark 2: The fitted trajectory serves as a bridge between the SC and controller, not only providing the controller with a motion-tracking target for the formation but also incorporating the SC information to offer the controller the ideal size of the formation. During the UAV formation guidance operation, the UGV is positioned inside the UAV formation's projection on the ground plane. When guiding through the obstacle region, the UAV formation changes its size to keep the UGV at a safe distance from the SC's edges.

D. Formation Tracking

To achieve the control objective in (5), the control input is defined as $\boldsymbol{u}_a = \dot{\boldsymbol{p}}_a$. The quantity $\bar{\boldsymbol{p}}_{ab}$ is defined as $\bar{\boldsymbol{p}}_{ab} = \boldsymbol{p}_a - \boldsymbol{p}_b$, $\bar{\boldsymbol{p}} = [\ldots, \bar{\boldsymbol{p}}_{ab}, \ldots] \in \mathbb{R}^{ml}$. The distance error e_{ab} between UAV a and UAV b in the formation is expressed as

$$e_{ab} = |\bar{\boldsymbol{p}}_{ab}| - d_{ab}. \tag{8}$$

Further, the derivative of e_{ab} is given by

$$\dot{e}_{ab} = \frac{|\bar{\boldsymbol{p}}_{ab}|(\boldsymbol{u}_a - \boldsymbol{u}_b)}{e_{ab} + d_{ab}} - \dot{d}_{ab} \tag{9}$$

The main results of the RGC are formally stated in the following theorem.

Theorem 1: Consider a formation consisting of n UAVs, where the tracking controller for each UAV is designed as $\boldsymbol{u} = R^{+}(\bar{\boldsymbol{p}})(-k_v z + d_v) + \boldsymbol{v}_d$. Every signal within this formation is

IEEE Robotics and Automation Letters (RA-L) paper, presented at ICRA 2026, Vienna, Austria. Cite as RA-L paper.

uniformly bounded across all states, and the formation error (8) for each UAV a will asymptotically approach zero.

Proof: The quantity z_{ab} is defined as

$$z_{ab} = |\bar{p}_{ab}|^2 - d_{ab}^2 = e_{ab}(e_{ab} + 2d_{ab}). \tag{10}$$

Based on z_{ab}, the Lyapunov function is chosen as

$$V(e,d) = \frac{1}{4}\sum_{(a,b)\in E^*} z_{ab}^2 = \frac{1}{4}z^T z, \tag{11}$$

where $e = [\ldots, e_{ab}, \ldots] \in \mathbb{R}^l$, $d = [\ldots, d_{ab}, \ldots] \in \mathbb{R}^l$ and $z = [\ldots, z_{ab}, \ldots] \in \mathbb{R}^l$. This function is positive definite in e and d, and its level surfaces $V(e,d) = a$ for some $a > 0$ are closed as $e_{ab} \geq -d_{ab}$.

Substituting (9) and (10) into (11), the time derivative of (11) is expressed as

$$\dot{V} = \sum_{a,b\in V^*} e_{ab}(e_{ab} + 2d_{ab})[\bar{\boldsymbol{p}}_{ab}^T(\boldsymbol{u}_a - \boldsymbol{u}_b) - d_{ab}\dot{d}_{ab}]. \tag{12}$$

Using (3), (4) and (11), (12) is simplified to

$$\dot{V} = z^T(\boldsymbol{R}(\bar{\boldsymbol{p}})\boldsymbol{u} - d_v), \tag{13}$$

where $d_v = [\ldots, d_{ab}\dot{d}_{ab}, \ldots] \in \mathbb{R}^l$, $\boldsymbol{u} = [\boldsymbol{u}_1, \ldots, \boldsymbol{u}_n] \in \mathbb{R}^{mn}$.

The following analysis, considering a formation $F(t) = (G^*, \boldsymbol{p}(t))$, lets the formation error $e(0) \in \theta_1$ when $t = 0$, where

$$\theta_1 = \left\{ e \in \mathbb{R}^l \mid \sum_{(a,b)\in E^*} e_{ab}^2 \leq \sigma \right\}, \tag{14}$$

and $\sigma \geq 0$. The control input $\boldsymbol{u}$ is denoted as

$$\boldsymbol{u} = \boldsymbol{R}^+(\bar{\boldsymbol{p}})(-k_v z + d_v) + \boldsymbol{v}_d, \tag{15}$$

where $\boldsymbol{R}^+(\bar{\boldsymbol{p}}) = \boldsymbol{R}^T(\bar{\boldsymbol{p}})[\boldsymbol{R}(\bar{\boldsymbol{p}})\boldsymbol{R}^T(\bar{\boldsymbol{p}})]^{-1}$, k_v is a positive control gain, and $\boldsymbol{v}_d = [\boldsymbol{v}_{d1}, \ldots, \boldsymbol{v}_{dn}]$, which denotes the formation maneuver speed. This ensures that (5) holds and $e = 0$ is exponentially stable.

Substituting (14) into (13) gives

$$\dot{V} = z^T[\boldsymbol{R}(\bar{\boldsymbol{p}})\boldsymbol{R}^+(\bar{\boldsymbol{p}})(-k_v z + d_v) + \boldsymbol{R}(\bar{\boldsymbol{p}})\boldsymbol{v}_d - d_v]. \tag{16}$$

For $\boldsymbol{v}_d$, $\boldsymbol{v}_{da} = \boldsymbol{v}_0 + \boldsymbol{\omega}_0 \times \bar{\boldsymbol{p}}_{an}$, where $a = 1, \ldots, n$, $\boldsymbol{v}_0$ represents the desired translational velocity, and $\boldsymbol{\omega}_0$ represents the desired angular velocity of the formation.

From (4) and (16), it follows that $R(\bar{\boldsymbol{p}})\boldsymbol{v}_d = 0$. Therefore, (16) is simplified to

$$\dot{V} = -k_v z^T z = -4k_v V. \tag{17}$$

Furthermore, it is derived that

$$\dot{V} \leq -4k_v\lambda_{\min} V \quad for \quad e(0) \in \theta_1, \tag{18}$$

where $\lambda_{\min}$ denotes the minimum eigenvalue of the matrix.

By analyzing (18), it is evident that $\dot{V}(t) \leq 0$ holds for any $t \geq 0$, which implies that $V(t)$ is non-increasing for any $t \geq 0$. Given that V is positive definite, $e = 0$ is exponentially stable for $e(0) \in \theta_1$. Therefore, the proof is complete.

Remark 3: Based on the fitted trajectory $T_r(t)$, the SC information is transformed into the controller input $F_r(t)$, and $\boldsymbol{v}$ is defined as $\boldsymbol{v} = \dot{T}_r(t)$. As the formation operates in a plane parallel to the ground, the parameters $d_v, \boldsymbol{v}_d$ in (15) are expressed as follows

$$\begin{cases} d_{ab}(t) = d_{ab}^* F_r(t) \\ \boldsymbol{v}_0 = \boldsymbol{v} \\ \boldsymbol{\omega}_0 = \frac{v_x\dot{v}_y - v_y\dot{v}_x}{v_x^2 + v_y^2} \times \bar{\boldsymbol{p}}_{ab}, \end{cases} \tag{19}$$

where v_x and v_y represent the x-axis and y-direction components of the vector $\boldsymbol{v}$, respectively. Using (19), the control inputs for each individual agent within the formation are denoted as

$$\boldsymbol{u}_a = \sum_{b\in V}(-k_v z_{ab} + d_{ab}\dot{d}_{ab}) + \boldsymbol{v}_0 + \boldsymbol{\omega}_0 \times \bar{\boldsymbol{p}}_{ab}, \tag{20}$$

where $a = 1, \ldots, n$.

IV. Validation & Analysis

In this section, the effectiveness validation of the scheme planner and controller was carried out. All validations were conducted on a 12th-generation Intel Core i5 CPU.

A. Plan Effectiveness Validation

The plan effectiveness validation was conducted on a randomly generated obstacle rasterized map measuring $400 \times 200\,\mathrm{m}^2$. The performance of the proposed waypoint planning method was assessed on this map, and comparative validation was performed using the A* method and the Theta* method.

In this scenario, the UAVs followed the movement of a virtual leader positioned at the center of the formation. The initial position of the virtual leader was $(1, 50)\,\mathrm{m}$, with the target point being $(400, 150)\,\mathrm{m}$. The UAVs' kinematic constraints on their trajectories were defined as $v_{\max} = 3.5\,\mathrm{m/s}$, $a_{\max} = 1\,\mathrm{m/s}^2$, $j_{\max} = 0.8\,\mathrm{m/s}^3$, $s_{\max} = 0.8\,\mathrm{m/s}^4$.

The validation employed the proposed method, the A* method, and the Theta* method. In the heuristic functions of the A* method and the proposed method, their weight coefficients were set to $k = 1.5$ and $q = 2.5$. For the Theta* method, the map was reconstructed with inflated obstacles, where the inflation size was set to 5 m.

The proposed SC and fitted trajectory are shown in Fig. 5(a), while the results of the A* and Theta* methods are presented in Fig. 5(b) and (c). The data indicate that the proposed method results in a smoother trajectory compared to the A* method and maintains a safer distance from obstacles compared to the Theta* method. Additionally, Fig. 6(d) depicts the size variation of the SC generated based on the three methods, and Fig. 6(a)–(c) illustrate the velocity, acceleration, and jerk profiles of each method's fitted trajectory. In Fig. 6(d), the SC generated by the proposed method remains stable at a larger size compared to that generated by the A* and Theta* methods. This implies that the proposed method facilitates smoother zoom-in and zoom-out maneuvers, thus enhancing formation stability. Fig. 6(a)–(c) demonstrate that the proposed method leads to smoother changes in velocity. The A* method produces numerous sharp turns in the trajectory, while the Theta* method results in excessive turning angles in the trajectory. Consequently, the proposed method demonstrates less variation in velocity and acceleration, leading to a more stable formation tracking of the trajectory.

As shown in Table I, the time complexity of the three methods was compared. Specifically, t_0, t_1, and t_2 represented the average execution time each method takes. Five simulations were conducted for each map size and the results were averaged. Compared to the A* method, the Theta* method adds the step of

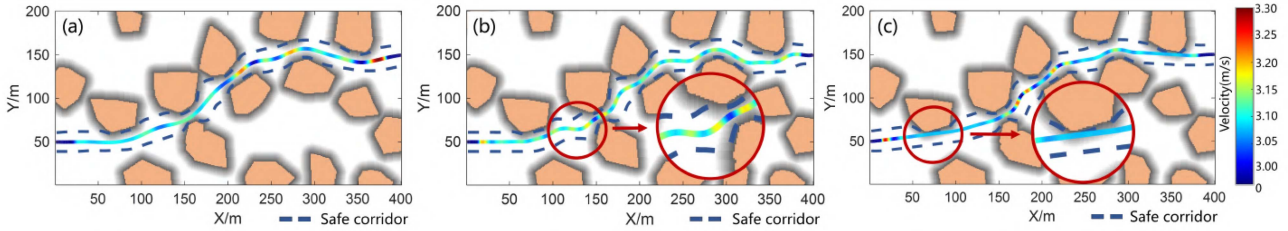

Fig. 5. Validation result of 2-D trajectory $T_r(t)$. (a) The proposed method. (b) A*. (c) Theta*.

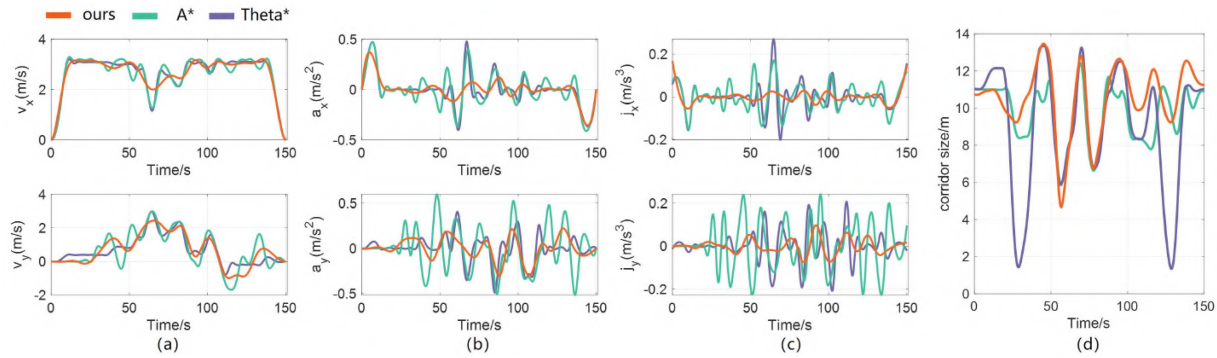

Fig. 6. 2-D trajectory motion information of the three methods. (a) Velocity. (b) Acceleration. (c) Jerk. (d) Safe corridor sizes.

TABLE I
ALGORITHM PERFORMANCE EVALUATION

Map Size (S/m^2)	Proposed Method (t_0/s)	A* (t_1/s)	Theta* (t_2/s)
400 × 200	1.009	0.987	1.256
500 × 250	1.071	1.043	1.468
600 × 300	1.136	1.097	1.715
700 × 350	1.305	1.112	1.935
800 × 400	1.428	1.235	2.172

TABLE II
TOTAL CONTROLLER SOLVING TIME

Scenario	FM			DF			DFM		
Numbers	3	5	7	3	5	7	3	5	7
RGC (t/ms)	213	322	458	210	330	494	214	343	499
[30] (t/ms)	211	326	469	210	348	522	211	357	524

LOS detection for waypoints connectivity, which significantly increases the time consumed. In contrast, the proposed method, by introducing the novel LOS mechanism, efficiently utilizes the maps searched by the A* method, consuming the same amount of time and yielding shorter waypoints. In the evaluation, the average execution time of the proposed method is comparable to that of the A* method, while the Theta* method's execution time increases proportionally with the map size, with a 76% increase in the largest map compared to the A* method.

B. Control Effectiveness Validation

As demonstrated in Table II, to validate the computational efficiency of RGC, three fixed-duration task scenarios were constructed in an ideal environment with specified time steps and a varying number of UAVs, including the formation maneuvering (FM) scenario, the dynamic formation (DF) scenario, and the dynamic formation maneuvering (DFM) scenario. The computational efficiency of the controller was evaluated by recording the total controller solving time in different scenarios. Additionally, comparative experiments were conducted using the method in [30]. In the validation, D, representing the total duration of the task, was set as $D = 100\,\text{s}$. Δt, denoting the time steps, was set as $\Delta t = 0.02\,\text{s}$, and the number of UAVs was set as $n = 3, 5, 7$. In the FM scenario, the maneuvering velocity function was: $\boldsymbol{v}_d = [0.3\sin(t), 0.3\cos(t), 0]$; in the DF scenario, the dynamic formation size function was: $AC = 0.5\sin(0.4t) + 1$; in the DFM scenario, the formation performed the motions simultaneously in the previous two scenarios. In Table II, the results show that the RGC computation time in the 3-UAV scenario is nearly identical to [30] (maximum difference: 3 ms). For 5-UAV and 7-UAV scenarios, RGC outperforms [30] with maximum differences of 28 ms, demonstrating superior efficiency.

Furthermore, to verify the RGC's robustness in obstacle-laden environments, control effectiveness and comparative validation with the method in [30] was performed in Unity.

The UAV's dynamics model was first constructed on the basis of (1) and (2). To reflect real-world conditions, a sensor interference term was introduced in Unity to account for errors in the UAV's position estimation. This interference included both sensor noise and random perturbation, expressed as $\boldsymbol{p}_M = \boldsymbol{p}_0 + \mathcal{N}(0, \sigma_s^2) + R(t)$, where $\boldsymbol{p}_M$ was the position measurement and $\boldsymbol{p}_0$ was the actual position. The random perturbation term, $R(t)$, was given by $R(t) = \beta \cdot R(t-1) + \varepsilon_t$, in which β represented the regression parameter, and ε_t was modeled as gaussian white noise with a mean of 0 and a variance of σ_ε^2. In the validation, the parameters were set as follows: $\sigma_s = 0.2$, $\sigma_\varepsilon^2 = 0.1$, $\beta = 0.6$.

The UAV formation consisted of five followers and a virtual leader located in its center. The formation topology is illustrated in Fig. 7(a), which was stabilized by controlling the relative

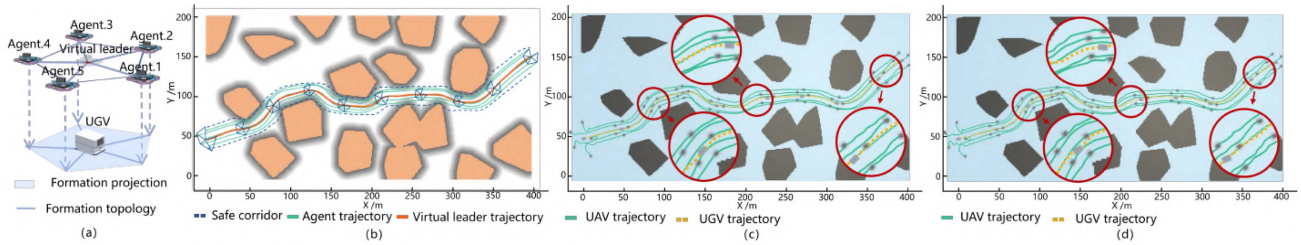

Fig. 7. Robustness validation of the formation controller. (a) Topological relationship of formation. (b) Ideal formation trajectory in Matlab. (c) Formation trajectory of RGC in unity. (d) Formation trajectory of [30] in unity.

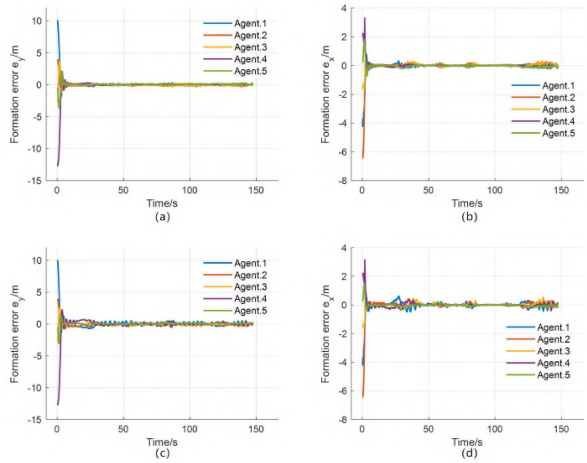

Fig. 8. Formation error for each agent in the robustness validation. (a) Formation error e_y of RGC. (b) Formation error e_x of RGC. (c) Formation error e_y of [30]. (d) Formation error e_x of [30].

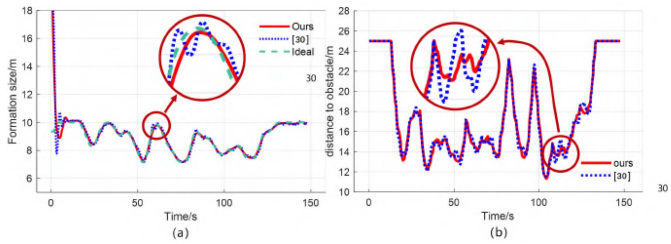

Fig. 9. UAV-UGV swarm's information in the robustness validation. (a) Comparison of ideal and actual UAV formation sizes. (b) UGV's distance to the obstacle.

distance between the corresponding UAVs, ideally forming a regular pentagonal shape. The UGV communicated with the UAVs to obtain their horizontal distances from itself, restricting its movement to the projected formation via a PID controller. To ensure effective formation guidance and maintain flight safety, the UAVs' dynamic feasibility constraints of their trajectories were defined as follows: $v_{\max} = 0.25\,\text{m/s}$, $a_{\max} = 0.3\,\text{m/s}^2$, $j_{\max} = 0.5\,\text{m/s}^3$ and $s_{\max} = 0.5\,\text{m/s}^4$.

During the validation, UAVs formed a formation from a chaotic initial state and guided the UGV to the target point, as shown in Fig. 7(a). The numerical validation of the UAV formation is illustrated in Fig. 7(b), while the dynamic validation of the proposed method, accounting for environmental disturbances in Unity, is illustrated in Fig. 7(c). For comparison, the validation result of [30] is illustrated in Fig. 7(d). The results demonstrate that the proposed method achieves more stable tracking performance with fewer trajectory fluctuations.

The position errors of the i-th UAV in formation, denoted as e_{xi} and e_{yi}, are shown in Fig. 8(a)–(d). To compare the effects of different controllers, the global mean absolute error (GMAE) and the formation synchronization error (FSE) were calculated. The GMAE quantifies the absolute deviation of the entire formation from the desired trajectory, reflecting the accuracy of formation tracking. The FSE measures the consistency of multi-UAV coordination, with a lower FSE indicating better formation stability. In validation, the proposed scheme yielded $GMAE_x = 0.043$ and $GMAE_y = 0.089$, with $FSE_x = 0.054$ and $FSE_y = 0.109$. In comparison, the method in [30] yielded $GMAE_x = 0.070$, $GMAE_y = 0.148$, $FSE_x = 0.091$, and $FSE_y = 0.188$. These results demonstrate that RGC exhibits better performance in both absolute tracking accuracy and formation stability. The variations of the ideal and actual formation sizes are depicted in Fig. 9(a). Unlike the formation controlled by the method in [30], the RGC-controlled formation reaches a steady state quickly and avoids fluctuations in formation size during the tracking process. Additionally, Fig. 9(b) illustrates the UGV consistently maintains a safe distance from the nearest obstacle under the guidance of the UAV formation. This result highlights the proposed scheme's effectiveness in formation guidance. In contrast, the results of [30], shown in Fig. 9(b), reveal fluctuations in the UGV's distance to obstacles due to instability in the formation size. This instability leads to excessive and unnecessary steering by the UGV. Consequently, the UGV's energy consumption rises. Compared to the APF method in [30], the RGC demonstrates superior robustness, maintaining a consistent and effective formation configuration throughout the trajectory tracking process. Furthermore, the smoother operation of UGVs under the proposed method reduces energy losses and improves overall efficiency.

V. Conclusion

This letter proposes a safety-aware UAV formation scheme to safely guide UGVs through obstacle-laden environments. The SC planning and formation tracking are bridged through the proposed SC-RGC formation, enabling formation maneuvering and dynamic adjustments within the SC. Compared to traditional methods, the novel SC planning method and the formation controller of the proposed scheme demonstrated better trajectory smoothness, higher planning efficiency, and superior formation stability.

Future work should explore leveraging UAV formations to guide multiple UGVs and conducting real-world experiments. This requires a detailed consideration of the collision avoidance problem among UGVs to ensure safe navigation. Furthermore, optimizing the UGVs' respective trajectories is imperative to minimize energy consumption.

REFERENCES

[1] X. Wang, W. Liu, Q. Wu, and S. Li, "A modular optimal formation control scheme of multiagent systems with application to multiple mobile robots," *IEEE Trans. Ind. Electron.*, vol. 69, no. 9, pp. 9331–9341, Sep. 2022.

[2] B. Ning, Q. Han, Z. Zuo, L. Ding, Q. Lu, and X. Ge, "Fixed-time and prescribed-time consensus control of multiagent systems and its applications: A survey of recent trends and methodologies," *IEEE Trans. Ind. Inform.*, vol. 19, no. 2, pp. 1121–1135, Feb. 2023.

[3] J. Tordesillas and J. P. How, "Mader: Trajectory planner in multiagent and dynamic environments," *IEEE Trans. Robot.*, vol. 38, no. 1, pp. 463–476, Feb. 2022.

[4] D. Zhou, Z. Wang, and M. Schwager, "Agile coordination and assistive collision avoidance for quadrotor swarms using virtual structures," *IEEE Trans. Robot.*, vol. 34, no. 4, pp. 916–923, Aug. 2018.

[5] J. Lin, Z. Miao, H. Zhong, W. Peng, Y. Wang, and R. Fierro, "Adaptive image-based leader-follower formation control of mobile robots with visibility constraints," *IEEE Trans. Ind. Electron.*, vol. 68, no. 7, pp. 6010–6019, Jul. 2021.

[6] C. Hu, Y. Hua, X. Dong, J. Yu, J. Lü, and Z. Ren, "Time-varying group formation tracking for multiagent systems with competition and cooperation via distributed nash equilibrium seeking," *IEEE Trans. Ind. Inform.*, vol. 20, no. 8, pp. 10054–10064, Aug. 2024.

[7] K.-K. Oh, M.-C. Park, and H.-S. Ahn, "A survey of multi-agent formation control," *Automatica*, vol. 53, pp. 424–440, 2015.

[8] J. Qi, J. Guo, M. Wang, C. Wu, and Z. Ma, "Formation tracking and obstacle avoidance for multiple quadrotors with static and dynamic obstacles," *IEEE Robot. Automat. Lett.*, vol. 7, no. 2, pp. 1713–1720, Apr. 2022.

[9] X. Xie, T. Sheng, and L. He, "Distributed event-triggered attitude consensus control for spacecraft formation flying with unknown disturbances and uncertainties," *IEEE Trans. Aerosp. Electron. Syst.*, vol. 58, no. 3, pp. 1721–1732, Jun. 2022.

[10] Y. Liu, S. Wang, Y. Xie, T. Xiong, and M. Wu, "A review of sensing technologies for indoor autonomous mobile robots," *Sensors*, vol. 24, no. 4, 2024, Art. no. 1222.

[11] W. Hönig, J. A. Preiss, T. S. Kumar, G. S. Sukhatme, and N. Ayanian, "Trajectory planning for quadrotor swarms," *IEEE Trans. Robot.*, vol. 34, no. 4, pp. 856–869, Aug. 2018.

[12] J. Chen, C. Du, Y. Zhang, P. Han, and W. Wei, "A clustering-based coverage path planning method for autonomous heterogeneous UAVs," *IEEE Trans. Intell. Transp. Syst.*, vol. 23, no. 12, pp. 25546–25556, Dec. 2022.

[13] Y. Wan, Y. Zhong, A. Ma, and L. Zhang, "An accurate UAV 3-D path planning method for disaster emergency response based on an improved multiobjective swarm intelligence algorithm," *IEEE Trans. Cybern.*, vol. 53, no. 4, pp. 2658–2671, Apr. 2023.

[14] N. Wang, J. Dai, and J. Ying, "UAV formation obstacle avoidance control algorithm based on improved artificial potential field and consensus," *Int. J. Aeronautical Space Sci.*, vol. 22, no. 6, pp. 1413–1427, 2021.

[15] H. Liu, X. Li, M. Fan, G. Wu, W. Pedrycz, and P. N. Suganthan, "An autonomous path planning method for unmanned aerial vehicle based on a tangent intersection and target guidance strategy," *IEEE Trans. Intell. Transp. Syst.*, vol. 23, no. 4, pp. 3061–3073, Apr. 2022.

[16] Y. Wang, Y. Yue, M. Shan, L. He, and D. Wang, "Formation reconstruction and trajectory replanning for multi-UAV patrol," *IEEE-ASME Trans. Mechatron.*, vol. 26, no. 2, pp. 719–729, Apr. 2021.

[17] S. Liu et al., "Planning dynamically feasible trajectories for quadrotors using safe flight corridors in 3-D complex environments," *IEEE Robot. Automat. Lett.*, vol. 2, no. 3, pp. 1688–1695, Jul. 2017.

[18] D. Mellinger and V. Kumar, "Minimum snap trajectory generation and control for quadrotors," in *Proc. IEEE Int. Conf. Robot. Automat.*, 2011, pp. 2520–2525.

[19] J. Park, D. Kim, G. C. Kim, D. Oh, and H. J. Kim, "Online distributed trajectory planning for quadrotor swarm with feasibility guarantee using linear safe corridor," *IEEE Robot. Automat. Lett.*, vol. 7, no. 2, pp. 4869–4876, Apr. 2022.

[20] J. Park, Y. Lee, I. Jang, and H. J. Kim, "DLSC: Distributed multi-agent trajectory planning in maze-like dynamic environments using linear safe corridor," *IEEE Trans. Robot.*, vol. 39, no. 5, pp. 3739–3758, Oct. 2023.

[21] J. Li et al., "A memetic path planning algorithm for unmanned air/ground vehicle cooperative detection systems," *IEEE Trans. Automat. Sci. Eng.*, vol. 19, no. 4, pp. 2724–2737, Oct. 2022.

[22] D. Yao, X. Wang, H. Lin, and Z. Wang, "Leader trajectory planning method considering constraints of formation controller," *J. Syst. Eng. Electron.*, vol. 34, no. 5, pp. 1294–1308, Oct. 2023.

[23] K. Ze, W. Wang, K. Liu, and J. Lü, "Time-varying formation planning and distributed control for multiple UAVs in clutter environment," *IEEE Trans. Ind. Electron.*, vol. 71, no. 9, pp. 11305–11315, Sep. 2024.

[24] W. Cheng, K. Zhang, and B. Jiang, "Fixed-time fault-tolerant formation control for a cooperative heterogeneous multiagent system with prescribed performance," *IEEE Trans. Syst. Man Cybern.*, vol. 53, no. 1, pp. 462–474, Jan. 2023.

[25] B. D. Anderson, C. Yu, B. Fidan, and J. M. Hendrickx, "Rigid graph control architectures for autonomous formations," *IEEE Control Syst. Mag.*, vol. 28, no. 6, pp. 48–63, Dec. 2008.

[26] D. V. Dimarogonas and K. H. Johansson, "Bounded control of network connectivity in multi-agent systems," *IET Control Theory Appl.*, vol. 4, no. 8, pp. 1330–1338, 2010.

[27] F. Mehdifar, C. P. Bechlioulis, F. Hashemzadeh, and M. Baradarannia, "Prescribed performance distance-based formation control of multi-agent systems," *Automatica*, vol. 119, 2020, Art. no. 109086.

[28] N. Funk, J. Tarrio, S. Papatheodorou, P. F. Alcantarilla, and S. Leutenegger, "Orientation-aware hierarchical, adaptive-resolution A$*$ algorithm for UAV trajectory planning," *IEEE Robot. Automat. Lett.*, vol. 8, no. 10, pp. 6723–6730, Oct. 2023.

[29] N. Wang and H. Xu, "Dynamics-constrained global-local hybrid path planning of an autonomous surface vehicle," *IEEE Trans. Veh. Technol.*, vol. 69, no. 7, pp. 6928–6942, Jul. 2020.

[30] Z. Pan, C. Zhang, Y. Xia, H. Xiong, and X. Shao, "An improved artificial potential field method for path planning and formation control of the multi-UAV systems," *IEEE Trans. Circuits Syst. II- Exp. Briefs*, vol. 69, no. 3, pp. 1129–1133, Mar. 2022.